Optimizing Interface Conductivity in Electronics

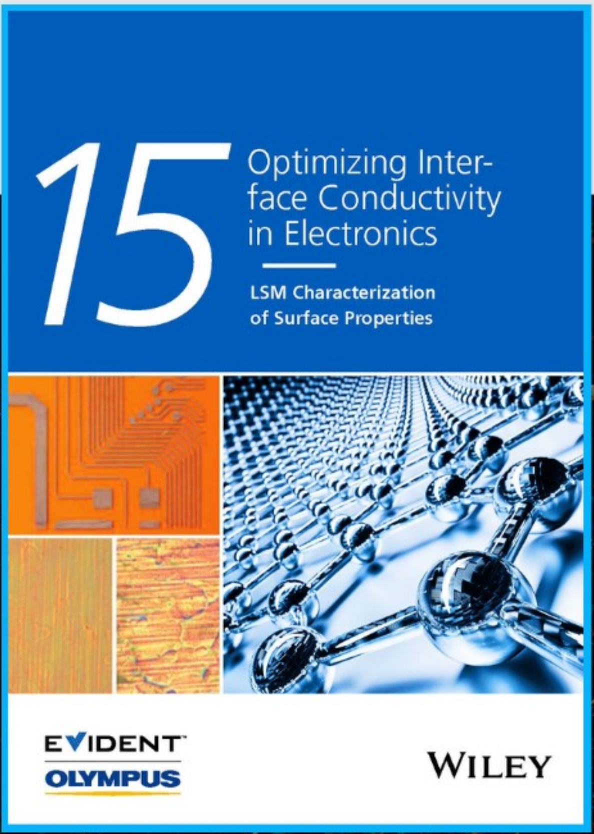

15

Optimizing Interface Conductivity in Electronics

LSM Characterization of Surface Properties

EVIDENT
OLYMPUS

WILEY

The latest eBook from Advanced Optical Metrology. Download for free.

Surface roughness is a key parameter for judging the performance of a given material's surface quality for its electronic application. A powerful tool to measure surface roughness is 3D laser scanning confocal microscopy (LSM), which will allow you to assess roughness and compare production and finishing methods, and improve these methods based on mathematical models.

Focus on creating high-conductivity electronic devices with minimal power loss using laser scanning microscopy is an effective tool to discern a variety of roughness parameters.

EVIDENT
OLYMPUS

WILEY

ADVANCED FUNCTIONAL MATERIALS
www.afm-journal.de

Noble Metal Ion-Directed Assembly of 2D Materials for Heterostructured Catalysts and Metallic Micro-Texturing

Joshua M. Little, Jiayue Sun, Ali Kamali, Amy Chen, Asher C. Leff, Yang Li, Leah K. Borden, Thilini U. Dissanayake, Deborah Essumang, Benita O. Oseleononmen, Dongxia Liu, Taylor J. Woehl, and Po-Yen Chen**

Assembling 2D-material (2DM) nanosheets into micro- and macro-architectures with augmented functionalities requires effective strategies to overcome nanosheet restacking. Conventional assembly approaches involve external binders and/or functionalization, which inevitably sacrifice 2DM's nanoscale properties. Noble metal ions (NMI) are promising ionic crosslinkers, which can simultaneously assemble 2DM nanosheets and induce synergistic properties. Herein, a collection of NMI–2DM complexes are screened and categorized into two sub-groups. Based on the zeta potentials, two assembly approaches are developed to obtain 1) NMI-crosslinked 2DM hydrogels/aerogels for heterostructured catalysts and 2) NMI–2DM inks for templated synthesis. First, tetraammineplatinum(II) nitrate (TPtN) serves as an efficient ionic crosslinker to agglomerate various 2DM dispersions. By utilizing micro-textured assembly platforms, various TPtN–2DM hydrogels are fabricated in a scalable fashion. Afterward, these hydrogels are lyophilized and thermally reduced to synthesize Pt-decorated 2DM aerogels (Pt@2DM). The Pt@2DM heterostructures demonstrate high, substrate-dependent catalytic activities and promote different reaction pathways in the hydrogenation of 3-nitrostyrene. Second, $PtCl_4$ can be incorporated into 2DM dispersions at high NMI molarities to prepare a series of $PtCl_4$–2DM inks with high colloidal stability. By adopting the $PtCl_4$–graphene oxide ink, various Pt micro-structures with replicated topographies are synthesized with accurate control of grain sizes and porosities.

1. Introduction

2D materials (2DMs), or nanosheets, are a class of nanomaterials and have drawn extensive attention due to their extraordinary chemical, physical, and mechanical properties, together with their chemical tunability and processable nature[1] 2DM nanosheets have been utilized as promising building block units for the fabrication of higher dimensional structures, which have been applied to catalysts,[2] electrochemical energy storage devices,[3] water desalination,[4] wearable electronics,[5] and soft robots.[6] However, during the self-assembly processes, 2DM nanosheets are prone to re-stack or aggregate due to their strong van der Waals forces, which decrease the accessible surface areas of assembled 2DM structures and sacrifice the nanoscale properties of 2DM units.[7]

To date, many fabrication strategies have been adopted to assemble 2DM nanosheets into higher dimensional structures (e.g., membranes, foams, aerogels) via incorporating molecular,[8] polymeric,[9] or nanoparticle additives,[10] inducing

---

J. M. Little, A. Kamali, Y. Li, L. K. Borden, T. U. Dissanayake,
D. Essumang, B. O. Oseleononmen, D. Liu, T. J. Woehl, P.-Y. Chen
Department of Chemical and Biomolecular Engineering
University of Maryland
College Park, MD 20742, USA
E-mail: tjwoehl@umd.edu; checp@umd.edu

J. Sun
Department of Chemistry and Biochemistry
University of Maryland
College Park, MD 20742, USA

The ORCID identification number(s) for the author(s) of this article can be found under https://doi.org/10.1002/adfm.202215222.

DOI: 10.1002/adfm.202215222

A. Chen
Department of Materials Science and Engineering
University of Maryland
College Park, MD 20742, USA

A. C. Leff
U.S. Army Combat Capabilities Development Command – Army Research Laboratory
Adelphi, MD 20783, USA

A. C. Leff
General Technical Services, LLC
Wall Township, NJ 07727, USA

P.-Y. Chen
Maryland Robotics Center
University of Maryland
College Park, MD 20742, USA

crosslinking reactions between 2DM nanosheets,[11] and utilizing supporter templates.[12] Although these approaches have created a variety of 2DM structures, the functionalities of 2DM nanosheets are either sacrificed or not scaled due to external binders/templates and surface functionalization. Featuring small sizes, high controllability, and strong electrostatic interactions, alkali earth metal ions and other accessible transition metal ions have emerged as effective ionic crosslinkers, enabling facile assembly of 2DM nanosheets into micro- or macrostructures for various applications.[13] For instance, Deng et al. adopted divalent (Mg^{2+}, Co^{2+}, Ni^{2+}, Fe^{2+}) and trivalent ions (Al^{3+}) to induce the gelation of $Ti_3C_2T_x$ MXene nanosheets (T_x referring to terminal groups such as —F, —O, and —OH), and the resultant MXene hydrogels were applied as the electrochemical electrodes in high-performance energy storage devices.[14] Also, Fe^{2+} has been selected by Liu et al. to mix with graphene oxide (GO) dispersion and form a highly stable Fe^{2+}–GO ink, which was used to facilitate the graphene-templated synthesis of tessellated Fe-oxide replicas.[15] While prior works focused on using alkali earth and transition metal ions to assemble 2DM nanosheets, incorporating these metallic species rarely provided additional functionalities. Noble metal ions (abbreviated as NMI) are promising yet less explored ionic crosslinkers, which can simultaneously assemble 2DM nanosheets and induce synergistic properties of NMI–2DM complexes.

Herein, a collection of NMI–2DM complexes was screened and categorized into two sub-groups based on their zeta potentials, and two assembly approaches were developed to fabricate 1) NMI-crosslinked 2DM hydrogels/aerogels for heterostructured catalysts and 2) NMI–2DM inks for templated synthesis. First, tetraammineplatinum(II) nitrate (TPtN) and tetraamminepalladium(II) nitrate (TPdN) were able to serve as efficient ionic crosslinkers to quickly agglomerate various 2DM dispersions. By utilizing micro-textured GO assembly platforms, various TPtN–2DM and TPdN–2DM hydrogels were fabricated in a facile and scalable fashion. Afterward, the TPtN–2DM hydrogels were freeze-dried and thermally reduced to synthesize various Pt-decorated 2DM aerogels (Pt@2DM). The Pt@2DM heterostructures demonstrated high, substrate-dependent catalytic activities and promoted different reaction pathways in the hydrogenation of 3-nitrostyrene (3-NS). Second, $PtCl_4$ and $AuCl_3$ were incorporated into 2DM dispersions at high ion molarities to produce a series of $PtCl_4$–2DM and $AuCl_3$–2DM inks, which were able to maintain high colloidal stability. By adopting the $PtCl_4$–GO inks, a graphene-templated synthetic route was demonstrated to fabricate various Pt replicas with accurate control of grain sizes and porosities.

2. Results and Discussion

2.1. Molecular Interactions of Noble Metal Ions (NMI) and 2D-Material (2DM) Nanosheets

In this work, three representative 2DM nanosheets, including GO, montmorillonite (MMT), and $Ti_3C_2T_x$ MXene, were adopted, and their TEM images are shown in Figure S1 (Supporting Information). The average diameters of GO, MMT, and MXene nanosheets were characterized to be ≈2 µm, ≈500 nm, and ≈2 µm, respectively. As shown in **Figure 1**a, the GO, MMT, and MXene dispersions demonstrated the average zeta potentials of <–30 mV, originating from the oxygen-containing and/or other

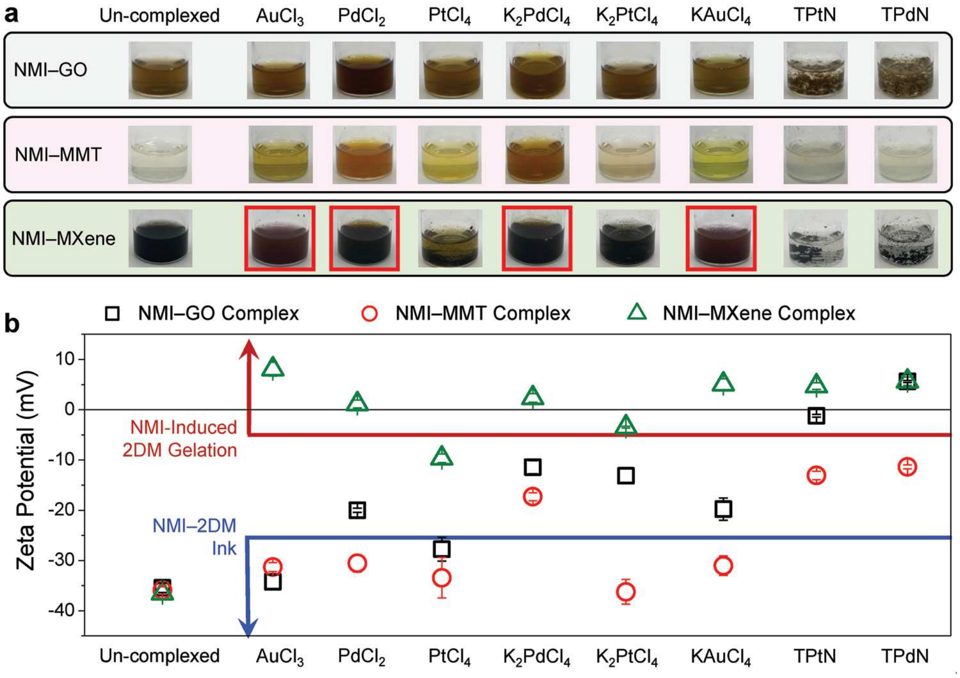

Figure 1. Screening of a collection of NMI–2DM complexes. a) Photos of un-complexed 2DM dispersions and a variety of NMI–2DM complexes. 2DM components include 0.1 mg mL^{-1} of GO, MMT, and $Ti_3C_2T_x$ MXene dispersions, and NMI components involve 5 mM of $AuCl_3$, $PdCl_2$, $PtCl_4$, K_2PdCl_4, K_2PtCl_4, TPtN, and TPdN solutions. b) Zeta potentials for a variety of NMI–2DM complexes. Red boxes: Unfavorable oxidation of MXene nanosheets or in situ formation of noble metal nanoparticles were observed in the K_2PdCl_4–MXene, $PdCl_2$–MXene, $AuCl_3$–MXene, and $KAuCl_4$–MXene complexes.

Table 1. Summary of average zeta potentials of NMI–2DM complexes. The NMI–2DM complexes with average zeta potentials >–10 mV are suitable for the NMI–induced 2DM gelation approach. The NMI–2DM complexes with average zeta potentials <–25 mV are suitable for the NMI 2DM ink approach. (*): Unfavorable oxidation of MXene nanosheets or in situ formation of noble metal nanoparticles are observed in the K_2PdCl_4–MXene, $PdCl_2$–MXene, $AuCl_3$–MXene, and $KAuCl_4$–MXene complexes. (**) Although the average zeta potentials of NMI–MMT complexes were slightly lower than –10 mV, freestanding MMT hydrogels were clearly observed.

Noble metal Ion (NMI)]	2D Material (2DM)	Zeta potential [mV]	2DM assembly method (Gelation vs NMI ink)
$Pt(NH_3)_4(NO_3)_2$	MXene	4.7 ± 0.7	NMI-Induced 2DM gelation
	GO	–1.2 ± 0.3	NMI-Induced 2DM gelation
	MMT	–13.1 ± 0.8**	NMI-Induced 2DM gelation**
$Pd(NH_3)_4(NO_3)_2$	MXene	5.7 ± 0.8	NMI-Induced 2DM gelation
	GO	5.6 ± 0.2	NMI-Induced 2DM gelation
	MMT	–11.4 ± 0.4**	NMI-Induced 2DM gelation**
$AuCl_3$	MXene	8.1 ± 1.4	MXene oxidation*
	GO	–34.2 ± 1.4	NMI 2DM ink
	MMT	–31.3 ± 0.9	NMI 2DM ink
$PdCl_2$	MXene	1.2 ± 0.8	MXene oxidation*
	GO	–20.0 ± 0.4	–
	MMT	–30.5 ± 1.7	NMI 2DM ink
$PtCl_4$	MXene	–9.7 ± 0.9	–
	GO	–27.7 ± 2.4	NMI 2DM ink
	MMT	–33.4 ± 6.0	NMI 2DM ink
K_2PdCl_4	MXene	2.3 ± 0.9	MXene oxidation*
	GO	–11.4 ± 1.3	–
	MMT	–17.3 ± 0.8	–
K_2PtCl_4	MXene	–3.5 ± 0.2	–
	GO	–13.1 ± 1.5	–
	MMT	–36.2 ± 2.5	NMI 2DM ink
$KAuCl_4$	MXene	5.1 ± 1.1	MXene oxidation*
	GO	–19.8 ± 2.2	–
	MMT	–31.0 ± 2.0	NMI 2DM ink

functional groups with strong negative dipoles on the surfaces of 2DM nanosheets (e.g., —COOH and —OH groups on GO; —OH groups on MMT; —F, —O, and —OH groups on MXene).[16]

Three kinds of 2DM dispersions were then mixed with various NMI solutions, and the resultant NMI–2DM complexes showed different colloidal behaviors with varying zeta potentials (Figure 1a,b, the NMI concentrations were kept at 5 mM). By setting two thresholds of >–5 mV and <–25 mV, these NMI–2DM complexes were categorized into two subgroups (**Table 1**). First, the TPtN–2DM and TPdN–2DM complexes showed immediate and irreversible agglomerations with average zeta potentials >–5 mV. On the other hand, the $PtCl_4$–GO, $PtCl_4$–MMT, $AuCl_3$–GO, and $AuCl_3$–MMT complexes maintained high colloidal stability, most of which exhibited average zeta potentials <–25 mV. Furthermore, it is worth mentioning that $Ti_3C_2T_x$ MXene nanosheets were oxidized in contact with K_2PdCl_4, $PdCl_2$, $AuCl_3$, and $KAuCl_4$, and noble metal nanoparticles were formed on the 2DM surfaces, as supported by the X-ray diffraction (XRD) spectra in Figure S2 (Supporting Information). There are several articles focusing on the oxidation of MXene nanosheets in O_2-saturated water,[17] but the time scale for this oxidation was at the week/month scale, much slower than the NMI-induced MXene oxidation (at the minute scale).

From the screening results above, it was clear that TPtN and TPdN had stronger intermolecular interactions with 2DM nanosheets and destabilized the resultant complexes, which can be explained as follows. The tetraamine groups of TPtN and TPdN are both strong hydrogen-bond acceptors and donors, which can interact with the hydrogen-bond donors (e.g., —COOH and —OH groups on GO, —OH groups on MMT,—OH groups on MXene) and hydrogen-bond acceptors (—F, and —O groups on MXene) on the surfaces of 2DM nanosheets.[9a] Additionally, the colloidal stability of NMI–2DM complexes is highly sensitive to the electrostatic interactions between 2DM nanosheets and NMI components. TPtN and TPdN are prone to dissociate the nitrate groups, forming $[Pt(NH_3)_4]^{2+}$ and $[Pd(NH_3)_4]^{2+}$ complex cations,[18] respectively. On the other hand, $AuCl_3$ and $PtCl_4$ are known to form $[AuCl_3(OH)]^-$ and $[PtCl_4(OH)]^-$, respectively. When different noble metal salts were added into the 2DM dispersion, the colloidal stability varied based on the overall net charges of NMI–2DM complexes. For instance, when TPtN was added, the negative charges of

2DM nanosheets were largely neutralized by the complexation of $[Pt(NH_3)_4]^{2+}$, and the TPtN–2DM complexes exhibited nearly zero net charges and irreversible agglomeration. On the other hand, the addition of $PtCl_4$ resulted in the complexation of 2DM nanosheets and $[PtCl_4(OH)]^-$, both of which exhibited negative charges and preserve high colloidal stability.[15,19] As both TPtN and TPdN served as effective ionic crosslinkers, low critical coagulation concentrations (CCCs) were observed, testing as low as 100 μM for the TPtN–2DM and TPdN–2DM complexes. As shown in **Figures 2–4**, an NMI-induced gelation method was developed to fabricate various NMI–2DM hydrogels and aerogels in a scalable manner without using any polymeric binders. On the other hand, the CCCs of $PtCl_4$–2DM and $AuCl_4$–2DM complexes were much higher at >10 mM. As shown in **Figure 5**, a variety of NMI-complexed 2DM inks demonstrated high colloidal stability even under high ion molarities, which were adopted for templated synthesis to enable microstructural metallic texturing with controllable topographies, grain sizes, and porosities.

2.2. Mechanically-Driven Fabrication of Crumple-Like GO Topographies as Versatile Assembly Platforms

Figure 2a illustrates the NMI-induced 2DM gelation method to fabricate various NMI–2DM hydrogels and aerogels, which involved four major steps: i) loading of NMI solutions onto crumple-like GO topographies, ii) upward diffusion of NMI into a deposited 2DM nanosheet suspension, iii) formation of NMI–2DM hydrogels, and iv) production of NMI–2DM aerogels via freeze drying.

To create the crumple-like GO topography, the GO dispersion was vacuum-filtered into a planar GO membrane followed by transferring it onto a thermally responsive polystyrene

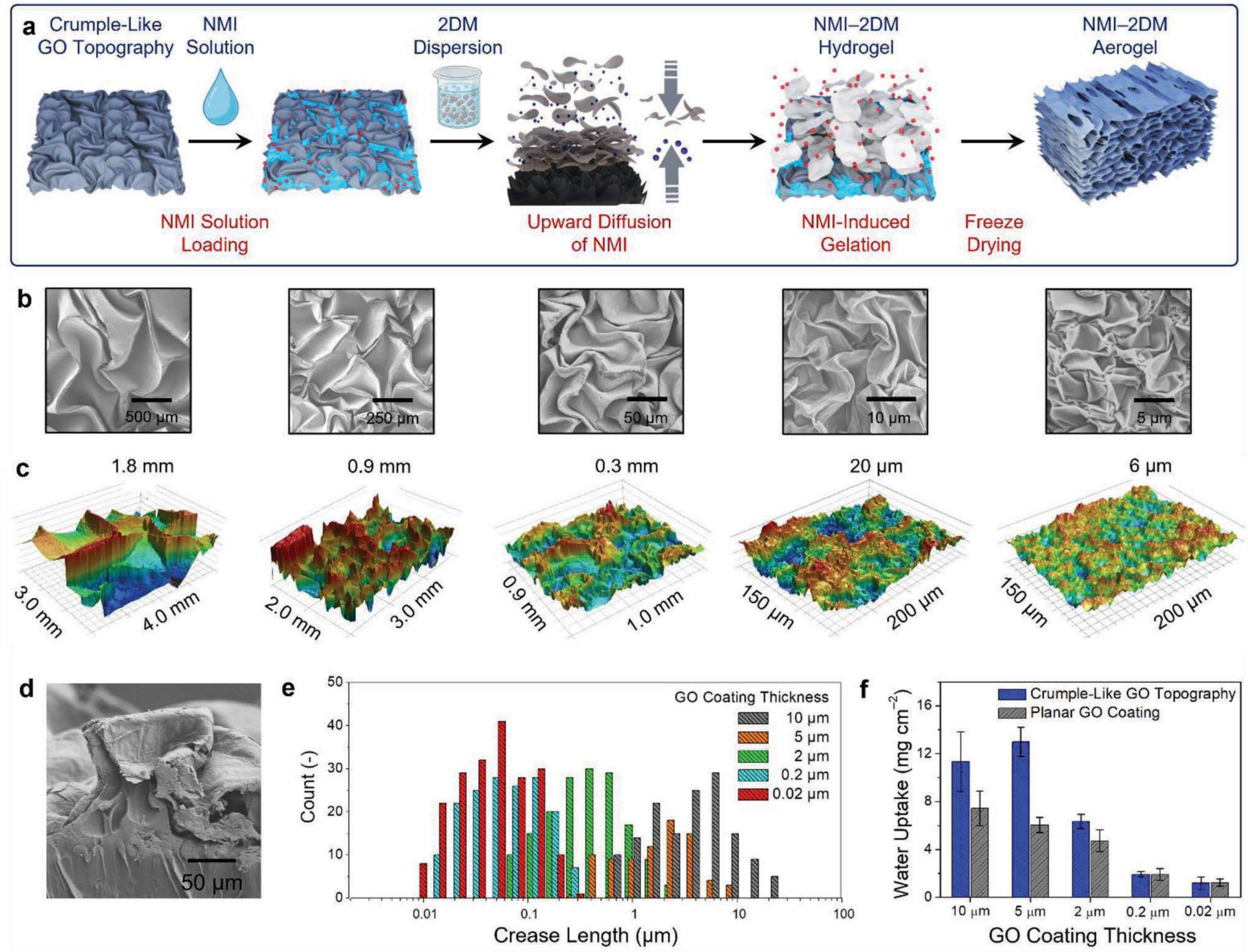

Figure 2. Mechanically-driven fabrication of crumple-like GO topographies as versatile assembly platforms. a) Schematic illustration of the scalable and versatile fabrication of various NMI–2DM hydrogels/aerogels through 1) loading of NMI solutions onto crumple-like GO topographies, 2) upward diffusion of NMI into a 2DM nanosheet dispersion, 3) formation of NMI–2DM hydrogels, and 4) production of NMI–2DM aerogels via freeze drying. b) Top-down SEM images and c) confocal laser images of various crumple-like GO topographies with different GO thicknesses of 10, 5, 2, 0.2, and 0.02 µm. d) Cross-section SEM image of a crumple-like GO topography on a shrunk polystyrene substrate. e) Crease length distributions of various crumple-like GO topographies with different coating thicknesses. f) Water adsorption capacities of crumple-like GO topographies with different thicknesses and their planar GO counterparts.

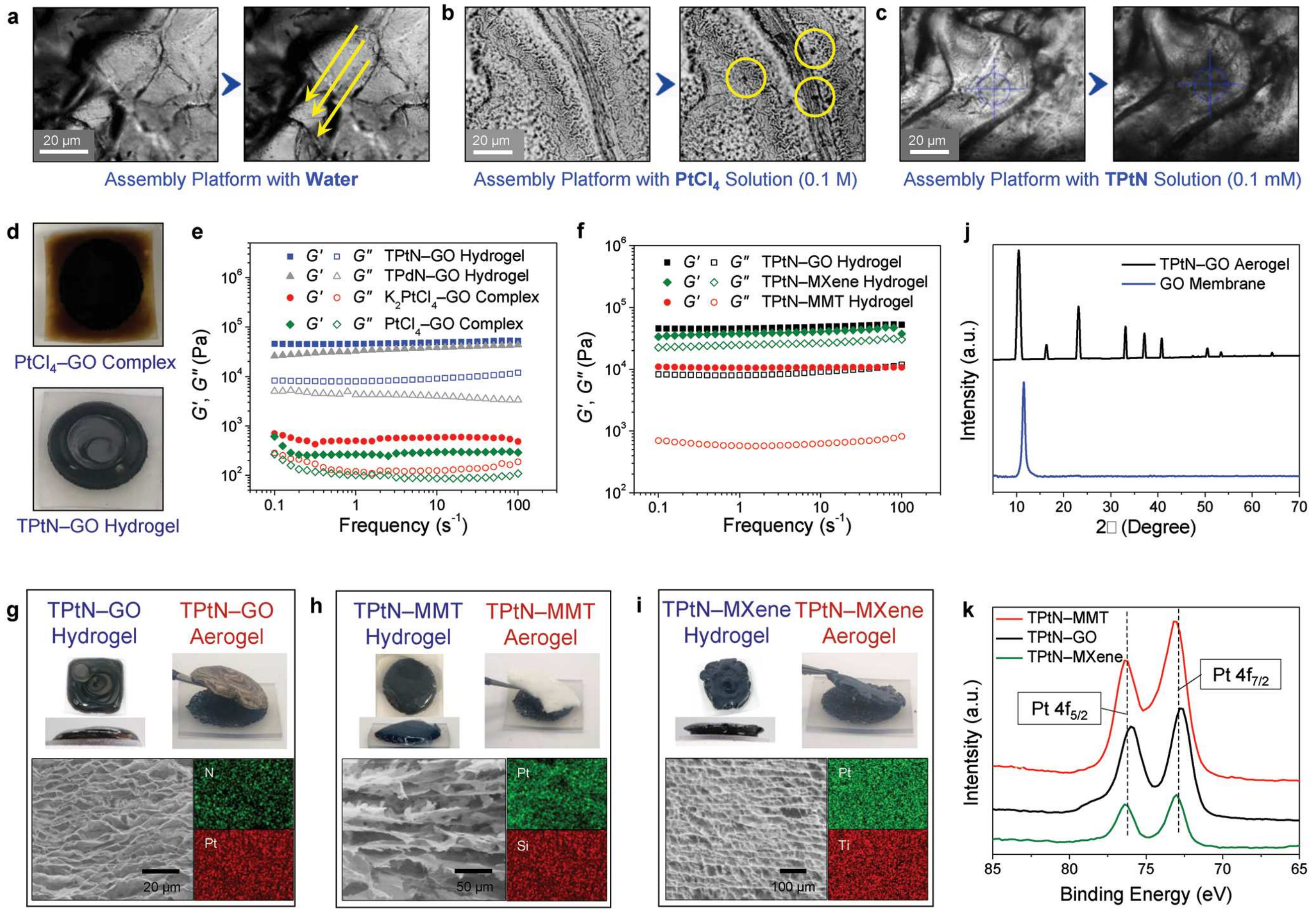

Figure 3. Facile fabrication of NMI–2DM hydrogels and aerogels via assembly platforms. IRM images of dilute GO dispersion (0.01 mg mL^{-1}) before and after dropping onto a) water-loaded GO platform, b) PtCl$_4$-loaded GO platform (0.1 M of PtCl$_4$ solution), and c) TPtN-loaded GO platform (1 mM of TPtN solution). d) Photos of a PtCl$_4$–GO complex and a TPtN–GO hydrogel. e) Storage (G') and loss moduli (G'') of TPtN–GO, PtCl$_4$–GO, and K$_2$PtCl$_4$–GO complexes. f) G' and G'' of TPtN–GO, TPtN–MMT, and TPtN–MXene hydrogels. Photos of g) TPtN–GO, h) TPtN–MMT, and i) TPtN–MXene hydrogels and aerogels. Inset: Cross-section SEM images and EDS mapping of TPtN–GO, TPtN–MMT, and TPtN–MXene aerogels. j) XRD analyses of a planar GO membrane and a TPtN–GO aerogel. k) XPS Pt 4f spectra of TPtN–GO, TPtN–MMT, and TPtN–MXene aerogels.

substrate (i.e., shrink film). The thermally responsive substrate was previously treated with atmospheric plasma to increase the surface hydrophilicity and enhance the adhesion energy between the GO membrane and polystyrene substrate.[20] As shown in Figure S3 (Supporting Information), by adjusting the areal loadings of GO nanosheets from 2.7 μg cm^{-2} to 1.8 mg cm^{-2}, the thicknesses of planar GO membranes were controlled from 0.02 to 10 μm, respectively. Afterward, the GO-coated shrink film was heated above the glass-transition temperature (T_g) of polystyrene (i.e., 100 °C) for 5–10 min, and the pre-strain was released to contract the underlying substrate into ≈20% of its original dimensions.[21]

By harnessing interfacial instability during substrate contraction, the upper-layer GO membrane was mechanically deformed into an out-of-plane architecture that displayed chaotic crumpling patterns. By controlling the thicknesses of GO membranes from 0.02 to 10 μm, the average size of crumpling patterns shifted from 3.0 × 1.0 μm^2 to 0.5 × 0.2 mm^2 (top-down scanning electron microscope (SEM) images in Figure 2b), and the average height of out-of-plane features varied from 6.0 μm to 1.8 mm (confocal laser images in Figure 2c), respectively. As shown in the cross-sectional SEM image in Figure 2d, the mechanically deformed GO layer was conformally attached to the shrunk polystyrene substrate, and the higher dimensional GO microstructure exhibited numerous valley-like micro-channels that benefit from high-capacity water adsorption.[22] By extracting the creases of crumple-like GO topographies from their top-down SEM images, their respective skeleton images are shown in Figure S4 (Supporting Information), and the crease length distributions are summarized in Figure 2e. As the thicknesses of GO membranes were controlled from 0.02 to 10 μm, the average crease length increased from 0.04 to 4.3 μm, respectively.

Furthermore, the water adsorption capacities of various crumple-like GO topographies (at different GO thicknesses) were characterized, and the planar GO membranes were used as control experiments. As shown in Figure 2f, the crumple-like GO topographies with interconnected water micro-channels demonstrated 1.5–2-times higher water uptake than the planar counterparts. When the GO thickness increased from 0.02 to 10 μm, the average water uptakes of crumple-like GO topographies increased from 1.2 to 11.3 mg cm^{-2}, respectively. When

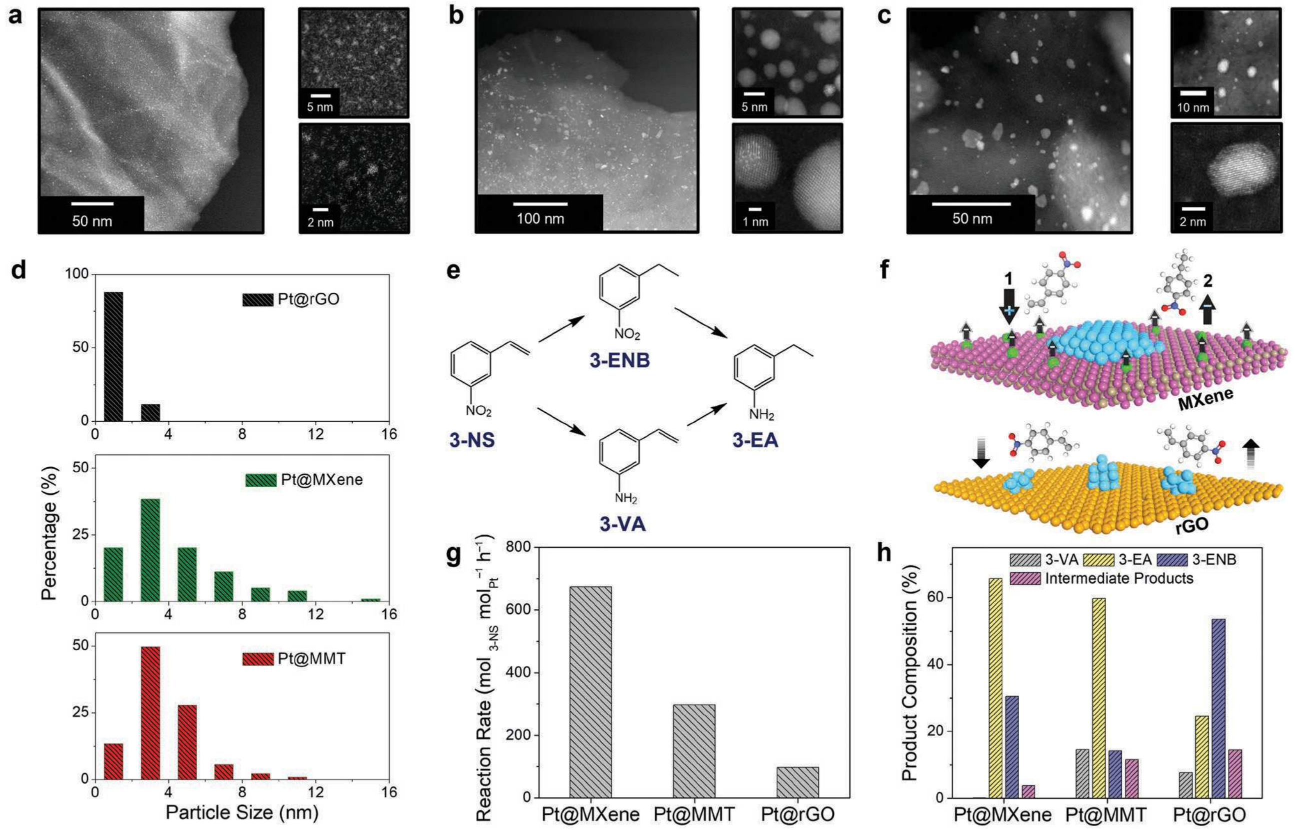

Figure 4. Growth of Pt nano-clusters/sheets on 2DM aerogels as heterostructured catalysts. HAADF STEM images of a) Pt@rGO, b) Pt@MMT, and c) Pt@MXene heterostructures. d) Particle size distribution of Pt nano-clusters/sheets on Pt@2DM aerogels. e) Reaction pathways of 3-NS hydrogenation. f) Schematic illustration of rapid electrostatically driven diffusion of 3-NS on Pt@MXene versus slow concentration gradient transport of 3-NS on Pt@rGO. g) Reaction rates of 3-NS using Pt@MXene, Pt@MMT, and Pt@rGO catalysts. h) Hydrogenated product percentages upon 80% conversion of 3-NS. (Reaction conditions: 0.6 mmol 3-nitrostyrene, 12 mL ethanol, 0.24 mmol 1-butanol, 0.01 g catalyst, 303 K, 3 bar.)

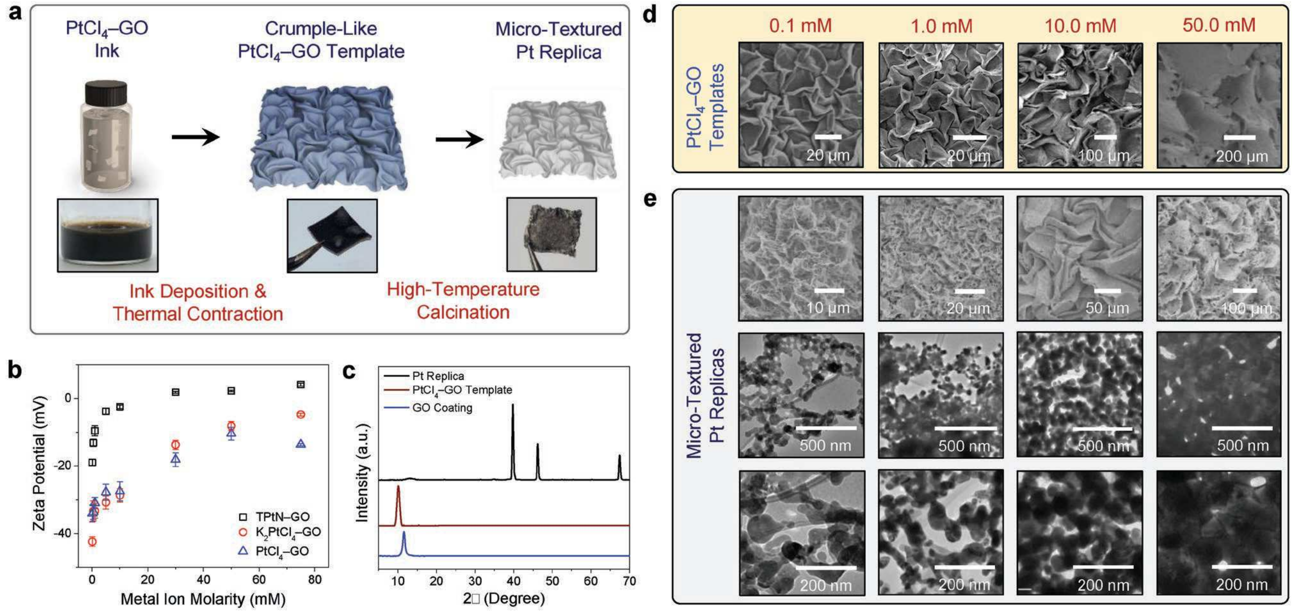

Figure 5. Pre-complexed NMI–GO inks for microstructural noble metal texturing. a) Schematic illustration and photos of the synthetic pathways of using $PtCl_4$–GO inks to fabricate micro-textured Pt replicas. b) Zeta potentials of TPtN–GO, $PtCl_4$–GO, and K_2PtCl_4–GO complexes at different salt molarities. c) XRD analyses of GO coating, $PtCl_4$–GO template, and Pt replica. d) Top-down SEM images of crumple-like $PtCl_4$–GO templates fabricated from the $PtCl_4$–GO inks with different $PtCl_4$ molarities. e) Top-down SEM images and TEM images of as-annealed Pt replicas produced from the $PtCl_4$–GO inks with different $PtCl_4$ molarities.

the GO thickness reached 5 μm, the resultant GO topography showed the highest water uptake of ≈13 mg cm^{-2} (equivalent to 14.7 g (of adsorbed water) g (of GO coating)$^{-1}$), which was close to some reported polymeric hydrogels.[23] It is worth mentioning that, although high water uptake of 11.3 mg cm^{-2} was observed in the 10-μm-thick case, its water uptakes were inconsistent due to heterogeneous substrate deformation (Figure S5, Supporting Information).

2.3. Facile Fabrication of NMI–2DM Hydrogels and Aerogels via Assembly Platforms

Benefitting from superior water uptakes (≈13 mg cm^{-2}), the crumple-like GO topographies (5-μm-thick) were able to serve as versatile assembly platforms, enabling facile fabrication of NMI–2DM hydrogels and aerogels without using polymeric binders. We chose GO nanosheets to create crumpled topographies primarily because of their inherent hydrophilicity. As shown in Figure S6 (Supporting Information), planar GO, MXene, and MMT membranes exhibited static contact angles of water (θ_w) below 90°, indicating hydrophilic surfaces. First, the crumple-like GO topographies were loaded with NMI solution (e.g., TPtN). Afterward, various 2DM dispersions, including GO, MXene, and MMT, were individually deposited onto the TPtN-loaded GO topographies, during which TPtN was gradually diffused out to form various TPtN–2DM hydrogels. As shown in Figure S7 (Supporting Information), all of the crumple-like GO, MXene, and MMT topographies were able to serve as efficient assembly platforms for creating thick TPtN–GO hydrogels.

As shown in Figure 3a,c, interference reflection microscopy (IRM) was employed to visualize the colloidal interactions between GO nanosheets and two NMI solutions, including $PtCl_4$ and TPtN. IRM utilizes a narrowband LED light source (511 nm here) along with placing the nanosheets close to an interface with a refractive index mismatch to generate a common path interferometer, which significantly enhances the image contrast enabling direct visualization of single layers of 2D materials (e.g., GO nanosheets). As shown in Movie S1 (Supporting Information) and Figure 3a, when a dilute dispersion of GO nanosheets was dropped onto the water-loaded assembly platform, the GO nanosheets (with the lateral dimensions of ≈2 μm) continuously flowed through the interconnected microchannels. As shown in Movie S2 (Supporting Information) and Figure 3b, when the GO dispersion was dropped onto the $PtCl_4$-loaded assembly platform (0.1 м of $PtCl_4$ solution), a few GO nanosheets were observed to attach onto the platform surface. As shown in Movie S3 (Supporting Information) and Figure 3c, when the GO dispersion contacted with the TPtN-loaded assembly platform (1 mм of TPtN solution), instantaneous coagulation of GO nanosheets was clearly observed. The results indicate that TPtN acted as an efficient ionic crosslinker and effectively screened the electrostatic double layers of GO nanosheets. As shown in Figure 3d and Figure S8 (Supporting Information), by following the NMI-induced gelation method, a thick, homogeneous, freestanding layer of TPtN–GO hydrogel was obtained on the assembly platform, while the $PtCl_4$–GO complex remained fluid-like and overflowed the assembly platform. Upon 24 h of air drying, the TPtN–GO film was readily detachable in the form of a flat and freestanding film (Figure S9, Supporting Information).

By utilizing the crumple-textured assembly platforms, a variety of NMI–GO complexes were prepared, including TPtN–GO, $PtCl_4$–GO, and K_2PtCl_4–GO, and their dynamic rheological behaviors were characterized. As shown in Figure 3e, the storage moduli (G') and loss moduli (G'') of a TPtN–GO hydrogel were characterized to be 5.0×10^4 and 2.5×10^4 Pa (over a frequency of 0.1 to 100 s^{-1}), respectively. In comparison, the G' and G'' of $PtCl_4$–GO and K_2PtCl_4–GO complexes were both 100 times lower. Figure 3f further demonstrates that the TPtN–GO hydrogel ($G' = 5.2 \times 10^4$ Pa) was stiffer than the TPtN–MXene ($G' = 3.7 \times 10^4$ Pa) and TPtN–MMT hydrogels ($G' = 1.0 \times 10^4$ Pa), which can be rationalized as follows. As GO and MXene possess rich oxygen-containing and/or other functional groups with strong negative dipoles (−COOH and −OH groups on GO; −F and −O groups on MXene),[16a,b,d] the coordinate bonds between tetraammineplatinum ions and 2DM nanosheets were relatively strong causing the hydrogels to exhibit a higher G'. In comparison, MMT nanosheets only possess some hydroxyl groups, so the TPtN–MMT hydrogel exhibited a lower G'.[16c] Second, the platinum cations interacted with the GO's aromatic frameworks through cation–π attractions, which further strengthened molecular interactions and thus led to the highest G'.[24]

Next, a freeze-drying step was conducted to transform TPtN–2DM hydrogels into aerogels. As shown in the SEM images in Figure 3g,i, all the TPtN–2DM aerogels exhibited cellular micro-structures with aligned open pores, templated by ice crystals during the freezing step. The pore size distribution profiles of three TPtN–2DM aerogels were analyzed via ImageJ. As illustrated in Figure S10 (Supporting Information), all of the TPtN–2DM aerogels had macroscale pores, with pore areas ranging from 5 to 500 μm^2 (TPtN–GO aerogel), 5 to 800 μm^2 (TPtN–MMT aerogel), and 5 to 1400 μm^2 (TPtN–MXene aerogel). Different 2DM nanosheets led to different pore sizes due to the differences in aspect ratios, hydrophilicity, and surface charge, all of which are critical during the lyophilization process.[25] As shown in the inset of Figure 3g,i, the energy-dispersive X-ray spectroscopy (EDS) maps confirmed that TPtN was uniformly distributed across the microstructures of TPtN–2DM aerogels. In Figure 3j, the XRD spectra reflected that, within the TPtN–GO aerogels, cubic NMI crystals (i.e., TPtN) were detected with low-intensity peaks at 17.5°, 24.2°, 33.2°, 37.1°, 40.8°, 50.5°, 53.4°, and 64.2°, while the (002) peak of GO multilayers remained at 11.6°. Afterward, XPS was employed to investigate the oxidation state of the platinum in the TPtN-GO aerogels. As shown in Figure 3k, the characteristic peaks representing Pt $4f_{7/2}$ and Pt $4f_{5/2}$ were observed at 73.0 and 76.2 eV, respectively, indicating that platinum ions remained in the 2+ oxidation state within the 2DM aerogels.[26] Figure S11 (Supporting Information) shows the survey scan of TPtN–GO aerogels. By increasing the GO thickness from 1 to 5 μm, the crumple size of the resulting GO topography increased from 20×15 to 100×75 μm^2, and the water adsorption capacities increased from 6.8 to 13.7 mg cm^{-2}, respectively. During the NMI-induced 2DM gelation process, the crumple-like GO topography with a higher adsorption capacity was able to load more NMI solution and induce the NMI–2DM hydrogels/aerogels with higher metallic loadings. As shown in Figure S12 (Supporting Information), by using a crumple-like assembly platform with the GO thickness of 5 µm, the resulting TPtN–GO aerogel demonstrated a TPtN loading of 33.5 wt.%, higher than the one fabricated using the platform with the GO thickness of 1 µm (20.8 wt.%).

2.4. Growth of Pt Nano-Clusters/Sheets on 2DM Aerogels as Heterostructured Catalysts

Next, the TPtN–GO, TPtN–MMT, and TPtN–MXene aerogels were thermally reduced at 250 °C in the forming gas (5% H_2 in N_2), and the Pt nano-clusters/sheets were in situ grown on the 2DM surfaces (abbreviated as Pt@2DM). Concurrently, the GO nanosheets were reduced into reduced GO (rGO). The SEM image of a Pt@rGO aerogel (after the thermal annealing process in the forming gas) is shown in Figure S13a (Supporting Information). Additionally, the pore size distribution profiles of TPtN–GO aerogel (before annealing, Figure S10a, Supporting Information) and Pt@rGO aerogel (after annealing, Figure S13b, Supporting Information) are compared, and both aerogels show similar pore size distribution profiles with the pore areas ranging from 5 to 500 µm^2. These results indicate the annealing step (and the reduction of TPtN) did not cause any significant microstructural contraction and pore shrinkage. Figure 4a,c shows the high-angle annular dark field (HAADF) scanning transmission electron microscope (STEM) images of Pt nanoparticles deposited on the 2DM aerogels, with the size distributions of Pt nanoparticles summarized in Figure 4d. All Pt@2DM heterostructures contained similar Pt loadings, estimated to be ≈9.5 wt.%. The Pt@rGO heterostructures primarily consisted of small Pt nanoclusters with an average diameter of 1.6 nm, containing several to a dozen Pt atoms each. On the other hand, the Pt@MMT and Pt@MXene heterostructures contained ultrathin Pt nanosheets with average diameters of 3.7 and 4.2 nm, respectively. It is worth noting that some larger Pt nanosheets (with diameters up to 15 nm) were found on the MXene surfaces. As further evidenced in the HAADF STEM images (in the inset of Figure 4b) and fast Fourier transform analyses (Figure S14, Supporting Information), the Pt nanosheets on MMT had uniform thicknesses, supported by constant image contrast across the Pt nanosheets. While the exact thickness was not known, the observation of bright single Pt atomic columns on top of the nanosheets indicated that the Pt nanosheets were likely single nanometers in thickness. Similarly, the Pt nanosheets on MXene were a few nanometers thick but possessed multiple layers of Pt that successively decreased in diameter, similar to the Tower of Hanoi.[27]

As all Pt@2DM aerogels were prepared through the same processes, these TEM images indicate that the Pt morphology was controllable by altering the underlying 2DM substrate, with the different surface functional groups and substrate compositions impacting the growth of Pt nano-clusters/sheets. Hard and soft acid and base theory has been previously used to rationalize the coordination of metal atoms on 2DM substrates and the effect of 2DM substrates on the observed Pt morphology.[28] Pt metal is a soft acid that most readily receives electrons from and binds most strongly to soft bases, such as thiolates, some halogens, and hydrocarbons, and less readily receives electrons from hard bases like hydroxide, carboxylate, and fluoride are weaker binding ligands. Based on the Pt morphologies observed by HAADF STEM, the binding strength between Pt atoms and 2DM substrates followed the order of Pt@rGO > Pt@MMT > Pt@MXene. The absence of Pt nanocrystals on rGO in favor of amorphous nanoclusters suggests that rGO-bound Pt atoms are most strongly among the three 2DM substrates. rGO consisted of a mixture of graphene regions, holes, and oxygen-containing defective regions,[29] where oxygen is mainly present in the graphene lattices in the form of C—O—C bonds.[30] Prior work has shown that weakly bound electrons from defects in the graphene lattice and oxygen-containing moieties act as soft bases and therefore coordination sites for metal atoms.[31] On the other hand, MMT is decorated with hydroxyl functional groups,[16c] which were hard bases that do not bind Pt atoms as strongly. The weaker binding strength between Pt and MMT allowed Pt atoms to crystallize and form 2D nanosheets. Finally, the MXene nanosheets were predominantly functionalized by fluorine groups,[16b,d] which have a larger chemical hardness than hydroxyl groups and therefore bound Pt atoms most weakly. Therefore, Pt nanoparticles began to take on some 3D character in the Pt@MXene aerogel by displaying multi-tier plate structures.

With distinct 2DM substrates and Pt morphologies, three Pt@2DM heterostructures displayed high, substrate-dependent catalytic activities. To determine the activities of Pt@2DM catalysts, the liquid-phase hydrogenation of 3-NS was selected as a probe reaction (Figure 4e), containing parallel reaction pathways to produce 3-ethylaniline (3-EA) via reaction intermediates 3-ethylnitrobenzene (3-ENB) and 3-vinylaniline (3-VA). As shown in Figure S15 (Supporting Information), control tests were performed using rGO, MMT, and MXene aerogels (also reduced at 250 °C in the forming gas) in the absence of Pt catalysts. In the same reaction timeframe (1 h), the MMT and rGO catalysts demonstrated low conversions of 3-NS at ≈10% and high selectivity toward the 3-ENB product, while the MXene catalyst showed higher conversion at ≈30% with high selectivity in forming 3-VA product, which cohered to the experimental observation in the literature.[32] The studies determined that the surface C—Ti—O_x groups and the layered structure of MXenes facilitate the mass transfer and adsorption–desorption processes which are responsible for the catalytic performance of $Ti_3C_2T_x$.[32a] In the presence of Pt catalysts, as shown in Figure 4g, the Pt@MXene, Pt@MMT, and Pt@rGO heterostructures demonstrated much higher catalytic activities with reactions rates of 674, 298, and 98 $\mathrm{mol_{3\text{-}NS}\ mol_{Pt}^{-1}\ h^{-1}}$, respectively. The dominating reaction pathway in these catalysts is the hydrogenation of the vinyl groups (—C=C) to form the 3-ENB and 3-EA products.

Both Pt morphologies and 2DM substrates had substantial impacts on the catalytic activities of Pt@2DM heterostructures. Taking Pt@rGO and Pt@MXene catalysts as examples, the Pt@rGO catalysts contained amorphous Pt nanoclusters with maximized exposure of active sites, and the Pt@MXene catalysts consisted of Pt nanosheets with multi-tier plate structures. Catalytic activities of supported Pt catalysts are reported to have a volcano-shaped relationship with the Pt particle sizes, in which the maximum activity appears at ≈1.0 nm Pt particle sizes.[33] Although the width of Pt nanosheets in the MXene substrate is assumed to lead to low catalytic activity, the thickness of Pt nanosheet (≈1.0 nm) seems to be a dominating factor that enabled the exceptionally high activities in the hydrogenation of 3-NS. The 2DM substrates also had critical effects on the activities of Pt@2DM catalysts. After the thermal treatment at 250 °C, the MXene surfaces preserved a large amount of electron-rich functional groups (e.g., $-$F, Ti$-$O), as evidenced in the XPS spectra (Figure S16a, Supporting Information). In contrast, the oxygen-containing groups of GO nanosheets were mostly removed after thermal treatment (Figure S16b, Supporting Information). As illustrated in Figure 4f, the electronegativity of MXene surfaces can attract the positively charged vinyl groups of 3-NS, favoring the hydrogenation of 3-NS by the surface/edge sites of Pt nanosheets via the hydrogen spillover effects.[34] On the other hand, the rGO surfaces lack prominent electronegative groups, so the adsorption of 3-NS to either rGO substrate or Pt nanoclusters was weak, retarding the catalytic activities in the hydrogenation of 3-NS.

With distinct Pt morphologies and 2DM electronegativities, three Pt@2DM catalysts promoted different reaction pathways in the hydrogenation of 3-NS. To understand the observed reaction selectivity, the adsorption behavior of 3-NS was interpreted via 1) the possible adsorption modes of 3-NS and 2) the adsorption strengths of two functional groups of 3-NS ($-$C=C and $-NO_2$). First, the adsorption mode of 3-NS is sensitive to the Pt structure.[35] As the dimensions of Pt nanocrystals decrease, the adsorption of vinyl groups ($-$C=C) can transit from the ethylidyne mode on threefold, the di-σ mode on twofold, and the π-bonded mode on isolated single atoms, with the adsorption strength in the rank of ethylidyne mode > di-σ mode > π-bonded mode.[36] When the Pt particle size is small enough such as single atoms, the supported Pt catalysts do not adsorb unsaturated vinyl groups, which leads to a high selectivity toward hydrogenation of the $-NO_2$ group in 3-NS.[37] In contrast, the adsorption of the nitro group ($-NO_2$) is not structure-dependent because $-NO_2$ has an end-on geometry, and the monodentate adsorption (rather than bidentate adsorption) is always preferred on the catalyst. For the electronic properties, the vinyl group is electron-rich, whereas the nitro group is electron-deficient, and thus nucleophilic sites on the catalyst will favor the adsorption of the nitro group, while repelling the vinyl group, and vice versa.[35]

When the conversion of 3-NS reached 80%, the percentages of various synthetic products, including 3-ENB, 3-VA, 3-EA, and intermediate products, were measured in Figure 4g. First, in the Pt@MXene catalysts, MXene's high electronegativity encouraged the interactions between vinyl groups of 3-NS and multitier Pt nanosheets. Upon adsorption, 3-NS can lay flat on the Pt nanosheets and fully hydrogenate. Figure S17 (Supporting Information) records the time profiles of synthetic products in the use of Pt@MXene catalysts, and the reaction pathway from 3-NS to 3-VA was highly prevented, showing 0% of 3-VA after 10 min of 3-NS hydrogenation. Second, in the Pt@MMT catalysts, MMT's mild electronegativity allowed either vinyl or nitro groups of 3-NS to be adsorbed on the Pt nanosheets followed by 3-NS hydrogenation, thus showing equal amounts of 3-VA and 3-ENB in the synthetic products. Last, in the Pt@rGO catalysts, the vinyl group of 3-NS adsorbed in either the di-σ or π-bonded mode, indicating that 3-NS did not lay flat on the Pt surfaces for full hydrogenation. The residual electron pairs after thermal reduction on rGO would repel the negatively charged $-NO_2$ group of 3-ENB, making it hard to re-adsorb on Pt nanoclusters for further hydrogenation.

2.5. Pre-Complexed NMI–GO Inks for Microstructural Noble Metal Texturing

Figure 5a shows the complexation method to prepare a series of NMI–2DM inks with high colloidal stability, including $PtCl_4$–GO, $AuCl_3$–GO, and $PtCl_4$–MMT inks (digital photos in Figure S18, Supporting Information). Specifically, the $PtCl_4$–GO ink was selected for templated synthesis of microstructural Pt topographies. By mixing a GO dispersion with a $PtCl_4$ solution at different concentrations (ranging from 0.1 to 50 mM), various $PtCl_4$–GO inks were prepared and deposited onto shrink films followed by overnight drying. The ink-coated substrates were then heated above the T_g of polystyrene (≈100 °C) to induce thermal contraction. By harnessing surface instability, the upper $PtCl_4$–GO coatings were mechanically deformed into isotropic crumples and became microstructural templates. Upon annealing and calcination at high temperatures, $PtCl_4$ was thermally reduced to Pt nanoparticles within the rGO multilayers followed by interlayer nanoparticle assembly. After the carbonaceous components were completely combusted at 800 °C, the resultant Pt replicas were able to resemble the crumple-like topographies from the $PtCl_4$–GO templates.

The success of this complexation method heavily relied on the high colloidal stability of $PtCl_4$–GO inks. As shown in Figure 5b, the zeta potentials of TPtN–GO, $PtCl_4$–GO, and K_2PtCl_4–GO complexes were characterized over a wide range of NMI molarities (from 0.1 to 75 mM). Compared to the TPtN–GO complexes that quickly flocculated, the $PtCl_4$–GO and K_2PtCl_4–GO complexes remained fluid-like at all tested molarities (up to 50 mM). To avoid the complication of K^+ counterions, the $PtCl_4$–GO complex was adopted for the templated synthesis of Pt replicas. Similar studies were conducted on the $AuCl_3$–GO and $PdCl_2$–GO complexes in Figure S19 (Supporting Information). By increasing the $PtCl_4$ molarities in the $PtCl_4$–GO inks, Young's moduli of $PtCl_4$–GO coatings increased accordingly (Figure S20, Supporting Information), and the crumpling wavelengths of $PtCl_4$–GO templates increased after thermal contraction, respectively (Figure S21, Supporting Information).

After the annealing and calcination processes in the air, the crumple-like topographies were transcribed from $PtCl_4$–GO templates to Pt replicas. As shown in the thermal gravimetric analysis (TGA) profiles in Figure S22 (Supporting Information), the GO template was partially decomposed at 150 °C and provided a spatially confined environment for the growth and assembly of Pt nanoparticles. At 450 °C, the rGO templates began to get oxidized into CO and CO_2. As the temperature was elevated to 800 °C, the rGO template was completely removed, leaving the freestanding Pt replica with resembled chaotic crumples (Figure 5e). It is worth mentioning that the presence of Pt nanoparticles slightly enhanced the carbon oxidation rates of the $PtCl_4$–GO sample, consistent with the experimental observation in the literature.[38] The TGA profile of an $AuCl_3$–GO template is shown in Figure S23 (Supporting Information); a similar profile is observed in comparison with PtCl4–GO, but the presence of Au nanoparticles does not enhance the carbon oxidation rates. High-temperature annealing and calcination processes of $PtCl_4$–GO templates yielded metallic Pt replicas, and three diffraction peaks at 40.3°, 46.7°, and 67.9° were observed in the XRD analysis (Figure 5c), which corresponded to the reflections (111), (200) and (220), respectively, and was consistent with the face-centered cubic structure of platinum (JCPDS Card 04–0802).

The characteristic crumpling features of Pt replicas were tunable by adjusting the $PtCl_4$ molarities in the $PtCl_4$–GO inks. When the $PtCl_4$–GO template (from the ink at 0.1 mм) was calcined, the resulting Pt product was non-continuous and did not well resemble the isotropic crumples. By increasing the $PtCl_4$ molarities to 1 and 10 mм, the Pt replicas were able to resemble fine microtextural features, while the crumpling wavelengths were reduced to 20%–50% of the wavelengths of $PtCl_4$–GO templates. When the $PtCl_4$ molarity increased further to 50 mм, the excess noble metal precursors overwhelmed the spatially confining effect and led to the appearance of a bulk metal phase.

To further characterize these underlying metallic nanostructures, we performed TEM analyses on these crumple-like Pt replicas in the inset of Figure 5e. As the $PtCl_4$ molarities in the $PtCl_4$–GO inks increased, the porosity of resulting Pt replicas continued to decrease. The Pt replica (from the ink at 10 mм) consisted of close-packed, interconnected, annealed Pt nanoparticle arrays. These TEM images provided mechanistic insights into the growth and assembly of Pt replicas. The thermal decomposition of $PtCl_4$–GO templates initially produces atomically dispersed Pt species or ultrafine clusters that are spatially confined in 2D gallery spaces. The existence of the rGO template through most of the annealing process causes preferential in-plane (x–y) mobility of these Pt clusters, so that the growth and annealing of Pt nanoparticles produce interconnected and array-like sub-structures that are the basic building blocks of the final Pt replicas. At higher temperatures, the rGO templates begin to decompose, gradually losing their spatial confinement effect to fully suppress z-directional expansion. The broad applicability of this approach was further illustrated by extending this templated synthesis to other noble metals (e.g., Au) (Figure S24, Supporting Information). The SEM and TEM images of microtextured Au replicas are shown in Figure S25 (Supporting Information). Compared to the microtextured Pt replica, the Au replica did not resemble the crumple-like microstructures of $AuCl_3$–GO templates to the same degree. The dampened replication capability may be due to the fact that Au nanoparticles had a high tendency to fuse together, thus losing some degrees of microstructural templating.

3. Conclusion

In summary, the use of NMI species for 2DM assembly demonstrated several advances to develop a collection of NMI–2DM complexes that retained the nanoscale functions of 2DM units and induced synergistic properties. Depending on the resultant zeta potentials, the NMI–2DM complexes were able to be fabricated into either mechanically robust hydrogels or electrostatically stable inks. First, by utilizing TPtN-loaded assembly platforms, various TPtN–2DM hydrogels and aerogels were produced in a facile manner. Followed by freeze drying and thermal reduction, various Pt@2DM heterostructures were synthesized and demonstrated high, substrate-dependent catalytic performance for 3-NS hydrogenation. Second, $PtCl_4$ was incorporated into 2DM dispersions to prepare a series of $PtCl_4$–2DM inks with high colloidal stability. By adopting the $PtCl_4$–GO ink, various Pt replicas with resembled topographies were synthesized with accurate control of grain sizes and porosities. It is worth noting that the Pt@MXene aerogels have promising potential in the field of heterostructured catalysts. From our perspective, an ideal hydrogenation catalyst that can achieve high activity and selectivity to 3-VA could be a heterostructure composed of single Pt atoms scattered across a negatively charged MXene substrate. First, when the Pt particle size decreases to only a few atoms, these tiny Pt catalysts become energetically unfavorable for adsorbing the unsaturated vinyl groups, leading to a high selectivity toward hydrogenation of the $-NO_2$ group in 3-NS. Second, since the $-NO_2$ group is electron-deficient, the MXene substrate should be functionalized with more negatively charged groups to facilitate the electrostatic diffusion of 3-NS to the surfaces of Pt@MXene catalysts. Future work will involve fine-tuning the Pt shape from 2D nanosheets to single atoms on the MXene surfaces to promote the adsorption of nitro groups over vinyl groups at higher diffusion rates. Additionally, understanding fundamental interactions between NMI species (and noble metals) and 2DM nanosheets is valuable for environmental applications, including wastewater treatment,[39] and electrochemical energy storage.[40]

4. Experimental Section

Materials: Gold(III) chloride ($AuCl_3$), potassium tetrachloroaurate(III) ($KAuCl_4$), palladium(II) chloride ($PdCl_2$), potassium tetrachloropalladate(II) (K_2PdCl_4), tetraamminepalladium(II) nitrate ($Pd(NH_3)_4(NO_3)_2$) (TPdN), platinum(IV) chloride ($PtCl_4$), potassium tetrachloroplatinate(II) (K_2PtCl_4), and tetraammineplatinum(II) nitrate ($Pt(NH_3)_4(NO_3)_2$) (TPtN), were purchased from Sigma-Aldrich and used as received. 3-nitrostyrene was purchased from Thermo Scientific and used as received. 1-butanol was purchased from Alfa Aesar and used as received. Ethanol was purchased from Pharmco and used as received. Ti_3AlC_2 MAX powders (Tongrun Info Technology Co. Ltd, China), sodium montmorillonite (MMT, BYK Additives Incorporation; Cloisite Na^+), and graphene oxide (GO) aqueous dispersion (Taiwan Graphene Company, 5 mg mL^{-1}) were used as received without further purification. Thermally responsive polystyrene shrink films were purchased from Grafix. Deionized (DI) water (18.2 MΩ) was obtained from a Milli-Q water purification system (Millipore Corp., Bedford, MA, USA) and used as the water source throughout the work.

Preparation of $Ti_3C_2T_x$ MXene Nanosheets: $Ti_3C_2T_x$ MXene nanosheets were prepared according to the previous work.[22] LiF (3.0 g) was added to 40 mL of 9.0 м HCl solution under vigorous stirring. After the dissolution of LiF, 1.0 g of $Ti_3Al_2C_2$ MAX powder was slowly added into the HF-containing solution, and the mixture was stirred at 35 °C for 24 h. Next, the suspension was split into two centrifuge tubes, and 5.0 mL of cold HCl solution (2.0 м) was added to each tube. The suspension was then centrifuged at 8000 rpm for 5 min, and the supernatant was replaced with cold HCl solution (2.0 м); this process was repeated three times. Afterward, the solid residue was washed with DI water multiple times until the pH value increased to ≈6.0. Subsequently, 35 mL of DI water was added to each tube to re-disperse the washed solid residue, and the mixture was sonicated for 1 h and centrifuged at 3000 r.p.m. for 30 min. The supernatant was collected as the final dispersion of $Ti_3C_2T_x$ MXene nanosheets with a concentration of ≈10–12 mg mL^{-1}.

Preparation of MMT Nanosheets: MMT nanosheets were prepared by mixing the as-received MMT crystals in DI water at 10 mg mL^{-1} followed by ultrasonication for 2 h and continuous stirring for 12 h. The dispersion was then centrifuged at 4000 rpm for 60 min, and the supernatant was collected as the final dispersion of MMT nanosheets with a concentration of ≈7 mg mL^{-1}. The MMT dispersion was diluted to 5 mg mL^{-1} for further usage.

Fabrication of Crumple-Like GO Topographies: A clear shrink film was cut into multiple squares with the dimensions of 10 × 10 cm^2 and cleaned with ethanol. Afterward, the cut shrink film was treated with atmospheric plasma (a Harrick Plasma expanded plasma cleaner composed of a borosilicate glass chamber and a 50–60 Hz, 373 W generator). The chamber pressure was pumped down to and maintained at 0.5–1.5 torr, and high radio frequency atmospheric plasma was generated for 5 min. To obtain a planar GO thin film with the controlled thickness varying from 0.2 to 10 μm, the areal loadings of GO nanosheets were adjusted accordingly on a hydrophobic polyvinylidene fluoride (PVDF) membrane (0.22 μm pore, Merck Millipore) followed by vacuum filtration for 8 hours. After air drying, the GO membrane was detached from the PVDF membrane in an ethanol bath and transferred onto a plasma-treated shrink film. Afterward, the GO-coated shrink film was heated in an oven at 150 °C for 7 min to induce thermal shrinkage. By harnessing interfacial instability, the upper-layer GO coating was deformed into the crumple-like GO topography, which was utilized as a versatile platform to assemble noble metal ions (NMIs) and 2D-material (2DM) nanosheets into NMI–2DM complexes.

Measurement of Water Storage Volumes on Crumple-Like GO Topographies: The crumple-like GO topographies were first weighed to obtain their dry masses. DI water was then dropped on the GO topographies, and excess water was then removed by tilting the substrate. The water-filled GO topographies were then weighed to obtain their wet masses. The difference between dry and wet masses was regarded as the water storage mass on a crumple-like GO topography. The water storage volumes were obtained by dividing the water storage mass by the water density. The measurement of water storage volumes was repeated multiple times.

Fabrication of NMI–2DM Hydrogels and Aerogels: Noble metal salt–2DM complexation hydrogels (abbreviated as NMI–2DM hydrogels) were prepared on the crumple-like GO topographies through a cation-induced gelation process. For each noble metal salt, the corresponding solution was prepared at 0.1 M, ≈150 μL of which was then deposited on top of a crumple-like GO topography with an area of ≈12 cm^2. The metal salt solution was allowed for 10 min to fully permeate the microchannels of the GO topography. After the surplus solution was removed, 3.0 mL of 2DM dispersion (at 10 mg mL^{-1}, ranging from GO, MXene, and MMT) was deposited on top of the GO topography in a swift motion, forming a thick, uniform NMI–2DM hydrogel layer. The NMI–2DM hydrogel then sat for 4 h to complete the ionic crosslinking reaction. The NMI–2DM hydrogel was then placed into a sealed petri dish and frozen with liquid nitrogen. The frozen sample was lyophilized in a freeze dryer (at –85 °C and 10^{-3} atm, Labconco FreeZone) for two days, obtaining an NMI–2DM aerogel.

In Situ Observation via IRM: In situ observation of NMI–2DM hydrogel formation was performed on an inverted Zeiss optical microscope. A field aperture with a size of 1 mm was placed in the back focal plane of the objective lens to limit the lens's numerical aperture and increase image contrast. A green LED with a wavelength of 511 ± 22 nm was used together with a 20× objective lens. Imaging was performed through a 0.17 mm glass coverslip to generate a common path interferometer, resulting from the light reflection off the glass-water interface.

A crumple-like MMT topography was first created by drop-casting an MMT dispersion onto a plasma-treated shrink film with an areal density of 1.0 mg cm^{-2}. Once air-dried, the planar MMT-coated shrink film was heated in an oven at 150 °C for 7 min to release the pre-strain to contract the underlying polystyrene substrate, and the upper-layer MMT coating was deformed into the crumple-like topography. The polystyrene substrate was then dissolved in a dichloromethane bath, and a freestanding MMT topography was transferred onto a glass slide. Next, the MMT topography received ≈100 μL of metal salt solution (0.1 M $PtCl_4$ and 1 mM TPtN) or deionized water and was then placed under IRM. Next, ≈10 μL of GO dispersion (at 1×10^{-3} mg mL^{-1}) was deposited onto the MMT topography, where IRM was recorded.

Preparation of Pt-Decorated 2DM Aerogels (Pt@2DM Aerogels): By utilizing the crumple-like GO topographies as the assembly platforms, TPtN–GO, TPtN–MXene, and TPtN–MMT aerogels were obtained and then thermally reduced in a tube furnace (OTF-1200X-S, MTI Corporation). Each TPtN–2DM aerogel was first placed in an alumina crucible inside a quartz tube. The tube furnace was then purged with forming gas (5% of H_2 and 95% of N_2) at 160 mL min^{-1} for 15 min. Last, the TPtN–2DM aerogel was reduced at 250 °C for 2 h, obtaining a Pt@2DM aerogel.

3-Nitrostyrene Hydrogenation Measurement: The catalytic performance of Pt@2DM aerogels was tested in a 50 mL stainless steel autoclave with an inner Teflon coating. For each test, 10 mg of a respective Pt@2DM aerogel was dissolved in 12 mL ethanol along with 0.6 mmol 3-Nitrostyrene (3-NS) and 0.24 mmol 1-Butanol as an internal standard. The reactor was then sealed and purged with 4 bar H_2 (Airgas, research grade) 3 times. Next, the reactor was pressurized to 3 bar, heated to 30 °C, and simultaneously stirred at 900 rpm. The products were then collected and filtered at pre-determined intervals using a syringe filter. The product solution was analyzed using a gas chromatography instrument (Agilent 7890A) equipped with a methylsiloxane capillary column (HP-1, 50.0 m × 320 μm × 0.52 μm) and a flame ionization detector (FID). The selectivity of products was calculated based on moles of product over the moles of reacted 3-NS.

Preparation of Noble Metal Salt–GO Inks (NMI–GO Inks): Various NMI–GO inks were prepared by mixing a GO dispersion (at 10 mg mL^{-1}) with solutions of noble metal salts (at 0.1 M of $AuCl_3$, $PtCl_4$) at different volume ratios. The concentration of noble metal ions was tuned from 0.1 to 50 mM.

Fabrication of Crumple-Like Noble Metal Topographies: The as-prepared NMI–GO ink was first drop-casted onto a plasma-treated shrink film at an areal density of 1 mg cm^{-2}. Once air-dried, the planar NMI–GO-coated shrink film was placed in between two baking sheets and then heated in an oven at 150 °C for 10 min to release the pre-strain to contract the underlying polystyrene substrate. Afterward, the resulting crumple-like NMI–GO topography was calcined at a high temperature in air for 2 h ($PtCl_4$–GO sample at 800 °C, $AuCl_3$–GO sample at 700 °C); the heating profile was set to be 5 °C min^{-1}. This obtained a crumple-like noble metal topography.

Characterization: The surface morphologies of crumple-like 2DM topographies, noble metal topographies, and NMI–2DM aerogels were investigated using a field emission scanning electron microscope (FESEM, Hitachi SU-70) operating at 10.0 kV for low, medium, and high-resolution imaging, equipped with an EDS for elemental analyses. Before SEM imaging, all the samples were sputtered with a layer of AuPd (≈1.0 nm). The 3D representations of crumple-like GO topographies were imaged by a Keyence microscope (VK-X3000 Series). Transmission electron microscopy (TEM) was performed using a JEM 2100 FEG TEM/STEM at an acceleration voltage of 200 kV. The noble metal topographies and NMI–2DM aerogels were suspended in ethanol and sonicated for 30 min, and then the dispersions were dropped on lacey carbon grids for TEM High-angle annular dark field scanning transmission electron microscopy (HAADF STEM) imaging was performed with a probe-corrected JEOL JEM-ARM200F TEM at an acceleration voltage of 200 kV. Thermogravimetric analysis (TGA) was carried out on a Shimadzu TGA-50 Series system, with the heating profile starting at 5 °C min^{-1} to 225 °C and then 10 °C min^{-1}. All of the TGA measurements were carried out under an N_2 flow rate of 60 mL min^{-1}, and the sample masses were controlled to be ≈20 mg.

The crystallinity of NMI–2DM aerogels and noble metal topographies were identified by XRD using a Bruker D8 Advance instrument with LynxEye detector and Cu Kα radiation (λ = 1.5418 Å). Rheology of various NMI–2DM hydrogels was evaluated with an AR2000 stress-controlled rheometer in between a 20-mm parallel plate and a conical plate at 25 °C. Dynamic frequency sweeps were performed in the linear viscoelastic region of each hydrogel sample. Zeta potentials of various NMI–2DM complexes were measured by a Nano-ZS90 Zetasizer (Malvern Instruments) with DTS1070 capillary cells. XPS was obtained by an X-ray photoelectron spectrometer (Kratos AXXIS UltraDLD) using a microfocused Al X-ray beam (100 µ, 25 W) with a photoelectron take-off angle of 90°.

Supporting Information

Supporting Information is available from the Wiley Online Library or from the author.

Acknowledgements

This work was partially funded by the Army Research Office under the Award No. #W911NF2010169 (U.D. and T.J.W.) and the National Science Foundation under the Grant No. 2045258 (A.C., J.S., and T.J.W.). This work was sponsored in part by the U.S. Army Combat Capabilities Development Command – Army Research Laboratory and was accomplished under an ARL Cooperative Research and Development Agreement (CRADA 14-052-22). The authors acknowledge the financial support provided by the Start-Up Fund of University of Maryland, College Park (KFS No.: 2957431 to P.-Y. Chen). Fundings for this research were provided by MOST-AFOSR Taiwan Topological and Nanostructured Materials Grant under Grant No. FA2386-21-1-4065 (KFS No.: 5284212 to P.-Y. Chen), and Energy Innovation Seed Grant from Maryland Energy Innovation Institute (MEI∧2) (KFS No.: 2957597 to P.-Y. Chen).

Conflict of Interest

The authors declare no conflict of interest.

Data Availability Statement

The data that support the findings of this study are available from the corresponding author upon reasonable request.

Keywords

2D materials, heterostructured catalysts, noble metal ions, noble metal nanocrystals, templated synthesis, $Ti_3C_2T_x$ MXene

Received: December 30, 2022
Revised: March 24, 2023
Published online:

---

[1] a) Y. Guo, K. Xu, C. Wu, J. Zhao, Y. Xie, *Chem. Soc. Rev.* **2015**, *44*, 637; b) D. Akinwande, C. J. Brennan, J. S. Bunch, P. Egberts, J. R. Felts, H. Gao, R. Huang, J.-S. Kim, T. Li, Y. Li, K. M. Liechti, N. Lu, H. S. Park, E. J. Reed, P. Wang, B. I. Yakobson, T. Zhang, Y.-W. Zhang, Y. Zhou, Y. Zhu, *Extreme Mech. Lett.* **2017**, *13*, 42; c) A. Gupta, T. Sakthivel, S. Seal, *Prog. Mater. Sci.* **2015**, *73*, 44.
[2] a) Y. Zhu, L. Peng, Z. Fang, C. Yan, X. Zhang, G. Yu, *Adv. Mater.* **2018**, *30*, 1706347; b) T. A. Shifa, F. Wang, Y. Liu, J. He, *Adv. Mater.* **2019**, *31*, 1804828.
[3] B. Mendoza-Sánchez, Y. Gogotsi, *Adv. Mater.* **2016**, *28*, 6104.
[4] S. Dervin, D. D. Dionysiou, S. C. Pillai, *Nanoscale* **2016**, *8*, 15115.
[5] a) O. A. Moses, L. Gao, H. Zhao, Z. Wang, M. Lawan Adam, Z. Sun, K. Liu, J. Wang, Y. Lu, Z. Yin, X. Yu, *Mater. Today* **2021**, *50*, 116; b) V. Orts Mercadillo, K. C. Chan, M. Caironi, A. Athanassiou, I. A. Kinloch, M. Bissett, P. Cataldi, *Adv. Funct. Mater.* **2022**, *32*, 2204772.
[6] L. Jing, K. Li, H. Yang, P.-Y. Chen, *Mater. Horiz.* **2020**, *7*, 54.
[7] a) X. Huang, C. Tan, Z. Yin, H. Zhang, *Adv. Mater.* **2014**, *26*, 2185; b) M. Zeng, Y. Xiao, J. Liu, K. Yang, L. Fu, *Chem. Rev.* **2018**, *118*, 6236.
[8] a) Z. Zeng, C. Wang, G. Siqueira, D. Han, A. Huch, S. Abdolhosseinzadeh, J. Heier, F. Nüesch, C. Zhang, G. Nyström, *Adv. Sci.* **2020**, *7*, 2000979; b) Y. Cai, J. Shen, G. Ge, Y. Zhang, W. Jin, W. Huang, J. Shao, J. Yang, X. Dong, *ACS Nano* **2018**, *12*, 56.
[9] a) H. Bai, C. Li, X. Wang, G. Shi, *J. Phys. Chem. C* **2011**, *115*, 5545; b) Z. Ling, C. E. Ren, M.-Q. Zhao, J. Yang, J. M. Giammarco, J. Qiu, M. W. Barsoum, Y. Gogotsi, *Proc. Natl. Acad. Sci. U. S. A.* **2014**, *111*, 16676.
[10] a) W. Yang, M. Pan, C. Huang, Z. Zhao, J. Wang, H. Zeng, *Compos. Commun.* **2021**, *24*, 100645; b) Y. Wang, Q. He, H. Qu, X. Zhang, J. Guo, J. Zhu, G. Zhao, H. A. Colorado, J. Yu, L. Sun, S. Bhana, M. A. Khan, X. Huang, D. P. Young, H. Wang, X. Wang, S. Wei, Z. Guo, *J. Mater. Chem. C* **2014**, *2*, 9478.
[11] C. N. R. Rao, K. Pramoda, R. Kumar, *Chem. Commun.* **2017**, *53*, 10093.
[12] Y. Shi, M. Osada, Y. Ebina, T. Sasaki, *ACS Nano* **2020**, *14*, 15216.
[13] a) X. Zhou, J. Wen, X. Ma, H. Wu, *J. Colloid Interface Sci.* **2022**, *624*, 505; b) P. Dutta, A. Sikdar, A. Majumdar, M. Borah, N. Padma, S. Ghosh, U. N. Maiti, *Carbon* **2020**, *169*, 225; c) U. N. Maiti, J. Lim, K. E. Lee, W. J. Lee, S. O. Kim, *Adv. Mater.* **2014**, *26*, 615.
[14] Y. Deng, T. Shang, Z. Wu, Y. Tao, C. Luo, J. Liang, D. Han, R. Lyu, C. Qi, W. Lv, F. Kang, Q.-H. Yang, *Adv. Mater.* **2019**, *31*, 1902432.
[15] M. Liu, P.-Y. Chen, R. H. Hurt, *Adv. Mater.* **2018**, *30*, 1705080.
[16] a) W. Cai, R. D. Piner, F. J. Stadermann, S. Park, M. A. Shaibat, Y. Ishii, D. Yang, A. Velamakanni, S. J. An, M. Stoller, J. An, D. Chen, R. S. Ruoff, *Science* **2008**, *321*, 1815; b) M. Naguib, M. Kurtoglu, V. Presser, J. Lu, J. Niu, M. Heon, L. Hultman, Y. Gogotsi, M. W. Barsoum, *Adv. Mater.* **2011**, *23*, 4248; c) J. B. Dixon, D. G. Schulze, *Soil mineralogy with environmental applications*, Soil Science Society of America Inc, Madison, WI **2002**; d) M. Naguib, V. N. Mochalin, M. W. Barsoum, Y. Gogotsi, *Adv. Mater.* **2014**, *26*, 992.
[17] a) C. J. Zhang, S. Pinilla, N. McEvoy, C. P. Cullen, B. Anasori, E. Long, S.-H. Park, A. Seral-Ascaso, A. Shmeliov, D. Krishnan, C. Morant, X. Liu, G. S. Duesberg, Y. Gogotsi, V. Nicolosi, *Chem. Mater.* **2017**, *29*, 4848; b) T. Wu, P. R. C. Kent, Y. Gogotsi, D. E. Jiang, *Chem. Mater.* **2022**, *34*, 4975; c) T. Habib, X. Zhao, S. A. Shah, Y. Chen, W. Sun, H. An, J. L. Lutkenhaus, M. Radovic, M. J. Green, *npj 2D Mater. Appl.* **2019**, *3*, 8.
[18] a) F. Jalilehvand, L. J. Laffin, *Inorg. Chem.* **2008**, *47*, 3248; b) J. Langlet, J. Bergès, J. Caillet, J. Kozelka, *Theor. Chem. Acc.* **2000**, *104*, 247.
[19] Z. Qin, H. Deng, R. Huang, S. Tong, *Chem. Eng. J.* **2022**, *428*, 132493.
[20] D. J. Guckenberger, E. Berthier, E. W. K. Young, D. J. Beebe, *Lab Chip* **2012**, *12*, 2317.
[21] K. Li, T.-H. Chang, Z. Li, H. Yang, F. Fu, T. Li, J. S. Ho, P.-Y. Chen, *Adv. Energy Mater.* **2019**, *9*, 1901687.
[22] M. Ding, S. Li, L. Guo, L. Jing, S.-P. Gao, H. Yang, J. M. Little, T. U. Dissanayake, K. Li, J. Yang, Y.-X. Guo, H. Y. Yang, T. J. Woehl, P.-Y. Chen, *Adv. Energy Mater.* **2021**, *11*, 2101494.
[23] a) G. Yilmaz, F. L. Meng, W. Lu, J. Abed, C. K. N. Peh, M. Gao, E. H. Sargent, G. W. Ho, *Sci. Adv.* **2020**, *6*, eabc8605; b) S.-L. Loo, L. Vásquez, A. Athanassiou, D. Fragouli, *Adv. Mater. Interfaces* **2021**, *8*, 2100580.
[24] D. A. Dougherty, *Acc. Chem. Res.* **2013**, *46*, 885.
[25] a) C. Zhu, T. Y.-J. Han, E. B. Duoss, A. M. Golobic, J. D. Kuntz, C. M. Spadaccini, M. A. Worsley, *Nat. Commun.* **2015**, *6*, 6962;

b) P. Rusch, D. Zámbó, N. C. Bigall, *Acc. Chem. Res.* **2020**, *53*, 2414; c) S. M. Jung, D. L. Mafra, C.-T. Lin, H. Y. Jung, J. Kong, *Nanoscale* **2015**, *7*, 4386.

[26] a) H. S. Kibombo, C.-M. Wu, R. Peng, J. Baltrusaitis, R. T. Koodali, *Appl. Catal., B* **2013**, *136*, 248; b) B. Ohtani, K. Iwai, S. Nishimoto, S. Sato, *J. Phys. Chem. B* **1997**, *101*, 3349.

[27] X. Yin, X. Liu, Y.-T. Pan, K. A. Walsh, H. Yang, *Nano Lett.* **2014**, *14*, 7188.

[28] a) R. D. Hancock, A. E. J. C. R. Martell, *Chem. Rev.* **1989**, *89*, 1875; b) M. P. Subbaiah, P. Kalimuthu, J. Jung, B.-H. Jeon, *J. Mater. Chem. A* **2021**, *9*, 18086; c) D. Grasseschi, W. C. Silva, R. d. Souza Paiva, L. D. Starke, A. S. do Nascimento, *Coord. Chem. Rev.* **2020**, *422*, 213469.

[29] K. Erickson, R. Erni, Z. Lee, N. Alem, W. Gannett, A. Zettl, *Adv. Mater.* **2010**, *22*, 4467.

[30] I. K. Moon, J. Lee, R. S. Ruoff, H. Lee, *Nat. Commun.* **2010**, *1*, 73.

[31] M. R. Axet, O. Dechy-Cabaret, J. Durand, M. Gouygou, P. Serp, *Coord. Chem. Rev.* **2016**, *308*, 236.

[32] a) M. M. Trandafir, F. Neațu, I. M. Chirica, Ş. Neațu, A. C. Kuncser, E. I. Cucolea, V. Natu, M. W. Barsoum, M. Florea, *ACS Catal.* **2020**, *10*, 5899; b) G. Bharath, K. Rambabu, A. Hai, I. Othman, N. Ponpandian, F. Banat, P. L. Show, *Chem. Eng. J.* **2021**, *414*, 128869; c) T. Hou, Q. Luo, Q. Li, H. Zu, P. Cui, S. Chen, Y. Lin, J. Chen, X. Zheng, W. Zhu, S. Liang, J. Yang, L. Wang, *Nat. Commun.* **2020**, *11*, 4251; d) M. López, Á. Morales-García, F. Viñes, F. Illas, *ACS Catal.* **2021**, *11*, 12850; e) H. Zhou, Z. Chen, A. V. López, E. D. López, E. Lam, A. Tsoukalou, E. Willinger, D. A. Kuznetsov, D. Mance, A. Kierzkowska, F. Donat, P. M. Abdala, A. Comas-Vives, C. Copéret, A. Fedorov, C. R. Müller, *Nat. Catal.* **2021**, *4*, 860.

[33] a) J. Li, B. Zhang, Y. Chen, J. Zhang, H. Yang, J. Zhang, X. Lu, G. Li, Y. Qin, *Catal. Sci. Technol.* **2015**, *5*, 4218; b) Y. Zhang, D. T. Tran, D. Baker, S. Zhang, T. Wang, S. Hwang, E. Schulman, J. Fu, W. Zheng, D. G. Vlachos, J. Qi, P. Christopher, Y. Liu, A. Frenkel, D. Liu, *Mol. Catal.* **2022**, *531*, 112709.

[34] J. Zhu, L. Xia, R. Yu, R. Lu, J. Li, R. He, Y. Wu, W. Zhang, X. Hong, W. Chen, Y. Zhao, L. Zhou, L. Mai, Z. Wang, *J. Am. Chem. Soc.* **2022**, *144*, 15529.

[35] L. Zhang, M. Zhou, A. Wang, T. Zhang, *Chem. Rev.* **2020**, *120*, 683.

[36] G. Hamm, T. Schmidt, J. Breitbach, D. Franke, C. Becker, K. Wandelt, *Zeitschrift für Physikalische Chemie* **2009**, *223*, 209.

[37] a) B. Han, Y. Guo, Y. Huang, W. Xi, J. Xu, J. Luo, H. Qi, Y. Ren, X. Liu, B. Qiao, T. Zhang, *Angew. Chem., Int. Ed.* **2020**, *59*, 11824; b) L. Liu, A. Corma, *Chem. Rev.* **2018**, *118*, 4981.

[38] P.-Y. Chen, M. Liu, T. M. Valentin, Z. Wang, R. Spitz Steinberg, J. Sodhi, I. Y. Wong, R. H. Hurt, *ACS Nano* **2016**, *10*, 10869.

[39] a) K. Yang, B. Chen, X. Zhu, B. Xing, *Environ. Sci. Technol.* **2016**, *50*, 11066; b) P. Zhao, M. Jian, Q. Zhang, R. Xu, R. Liu, X. Zhang, H. Liu, *J. Mater. Chem. A* **2019**, *7*, 16598.

[40] L. Peng, Z. Fang, Y. Zhu, C. Yan, G. Yu, *Adv. Energy Mater.* **2018**, *8*, 1702179.